Article

Experimental Investigation of Infrared Detection of Debonding in Concrete-Filled Steel Tubes via Cooling-Based Excitation

Haonan Cai [1] and **Chongsheng Cheng [1,2,*]**

1   School of Civil Engineering, Chongqing Jiaotong University, Chongqing 400074, China;
    611210080005@mails.cqjtu.edu.cn
2   State Key Laboratory of Mountain Bridge and Tunnel Engineering, Chongqing Jiaotong University,
    Chongqing 400074, China
*   Correspondence: ccheng@cqjtu.edu.cn

Abstract: Debonding in concrete-filled steel tubes (CFSTs) is a common defect that often occurs during the construction phase of CFST structures, significantly reducing their load-bearing capacity. Current methods for detecting debonding in CFSTs using infrared thermography primarily rely on heat excitation. However, applying this method during the exothermic hydration phase presents considerable challenges. This paper proposes the innovative use of spray cooling as an excitation method during the exothermic hydration phase, providing quantitative insights into the heat conduction dynamics on steel plates for infrared debonding detection in CFSTs. The effects of atomization level, excitation distance, excitation duration, and water temperature in the tank on infrared debonding detection performance were examined. The timing of the maximum temperature difference under cooling excitation was analyzed, and the heat conduction characteristics on the surface of the steel plate during the cooling process were explored. A highly efficient and stable cooling excitation method, suitable for practical engineering detection, is proposed, providing a foundation for quantitative infrared debonding detection in CFSTs. This method does not require additional energy sources, features a simple excitation process, and results in a five-times increase in temperature difference in the debonded region after excitation.

Keywords: concrete-filled steel tube (CFST); infrared debonding detection; exothermic hydration phase; spray-cooling excitation

1. Introduction

CFSTs, which are hybrid structures consisting of high-strength steel encasing concrete, have found extensive applications in buildings and bridge engineering due to their exceptional mechanical performance and structural efficiency [1–4]. These structures offer significant benefits, including a high load-bearing capacity, ease of construction, and superior seismic performance. However, debonding between the steel tube and concrete in CFSTs is a common issue that undermines the synergy of the composite material, thereby diminishing its mechanical properties [5–11]. Yang et al. [9] reported that the mechanical performance of CFSTs decreases when the extent of debonding exceeds 0.0757%. When debonding occurs, the load-bearing capacity of CFST components can decrease by 10–32.1%, and the modulus can decline by 30–53% [5–8]. Furthermore, Lu et al. [10] observed that debonding can alter a bridge's natural frequency, affecting its dynamic performance. Thus, debonding in CFSTs is a critical concern for the safety and longevity of these structures.

During the construction phase, debonding in CFSTs may result in large voids due to factors such as air bubble migration and concrete bleeding [12]. Han et al. [8] observed that air may not be expelled efficiently during the concrete filling process, leading to residual bubbles and subsequent void formation. Additionally, Chen et al. [13] identified concrete bleeding as a key factor in void development in CFSTs during arch bridge construction. While methods such as vibration and hammering can mitigate void formation during construction, they become ineffective once the concrete solidifies. Post-solidification repairs typically involve invasive procedures such as drilling and grouting [12]. Therefore, the timely and accurate detection of debonding in CFSTs during construction is crucial to prevent the need for such damaging repair methods and ensure structural integrity.

Infrared thermography stands as a nondestructive detection technique useful in identifying debonding in CFSTs. This method analyzes discrepancies in the temperature field across the CFST surface [14–16]. Its advantages over traditional methods, such as ultrasound [17], impact echo techniques [18] and acoustic emission [19], include noncontact operation and heightened efficiency. Due to the high detection efficiency, fast detection speed, and long detection distance of infrared defect detection technology, many researchers have recently conducted studies on infrared thermal imaging-based debonding detection in CFSTs [20,21]. A crucial step in enhancing the visibility of defects in infrared thermography is the application of manual active excitation during testing [22–27]. Predominantly, these excitation methods involve various heating techniques, including microwave heating [22], laser heating [23,24], and pulse heating [26,28,29]. These techniques have been extensively researched, focusing on aspects such as excitation distance, uniformity, and duration, as well as post-excitation visualization in the domain of defect detection in metal materials using infrared thermography. Deane et al. [25] employed a 250 W lamp as a thermal source, analyzing the resulting infrared images using techniques such as pulsed phase thermography transforms, the principal component technique, and cold image subtraction. Addressing the challenge of uneven illumination in infrared thermal wave nondestructive testing, Li et al. [26] developed an optimized optical model, ensuring uniform irradiance distribution on curved surfaces. Further advancing the field, Xu et al. [24] introduced a novel method that utilizes an optical excitation line laser as a heat source in infrared thermal imaging. This technique, specifically designed for debonding detection in fiber-reinforced polymer-reinforced concrete structures, overcomes the limitations inherent in traditional infrared methods, such as short heating distance, low thermal sensitivity, and high power requirements.

Most research on CFSTs has historically focused on testing during the operational phase, where exothermic hydration is not a factor [30,31]. Currently, research on conducting semi-real-time infrared tests during the hydration heat phase of CFSTs remains insufficient. During this phase, the hydration of concrete within the steel tube releases significant heat, which may compromise the reliability of traditional thermal excitation methods [30,31]. Li et al. [31] explored using infrared thermography to detect grouting defects in external prestressed tendon ducts during exothermic hydration. Their research, involving semi-real-time infrared tests conducted within 48 h after grouting, demonstrated the method's feasibility. Furthermore, Yang et al. [32] examined the effectiveness of infrared thermography in detecting CFST debonding under varying temperature conditions, simulating the exothermic hydration process of concrete at different water temperatures. Their findings indicated the successful identification of large defects, though smaller ones were overlooked. Additionally, they validated the use of water to simulate concrete's exothermic hydration through ANSYS simulations. Despite these advancements, no studies have yet incorporated external active excitation during the CFST hydration process. Cheng et al. [33] demonstrated that, when CFST is in the construction stage, using the concrete's hydration

heat as an internal heat source can effectively enable infrared debonding detection. Factors such as debonding size, hydration heat temperature rise rate, and ambient temperature all influence detection efficiency. Cai et al. [34] found that during the heat absorption and release phases of debonding in CFSTs, the infrared images of the debonding region exhibit different characteristics. The infrared thermal contrast is linearly correlated with the interfacial heat flux of the CFST. When CFST is in the hydration heat phase, the heat from the CFST conducts outward. If heating excitation is applied at this time, the interfacial heat flux of the CFST will approach zero, inhibiting outward heat conduction and ultimately hindering infrared debonding detection.

Therefore, the active excitation of CFST in the hydration heat stage by cooling can enhance the outward conduction of CFST heat, thus improving the infrared detection capability. Cai et al. [35] proved the feasibility of using spray cooling as the excitation source to actively stimulate CFST in the hydration heat stage through model tests, and defined the relationship between the excitation strength and the temperature difference in the debonding area through finite element simulation. However, this process involves the spraying of mist or water to absorb and dissipate thermal energy, with the underlying heat transfer mechanisms being notably complex [36–38]. Pais et al. [39] identified four primary mechanisms in spray cooling: evaporation, forced convection, nucleation sites on heated surfaces, and secondary nucleation sites on droplet surfaces. Yan et al. [40] emphasized the superior cooling efficiency of spray cooling compared to other methods, with Pais et al. [39] demonstrating that its highest heat flux density can reach 1200 W/cm^2. However, the cooling efficiency is influenced by factors such as the atomization level of the water flow [41]. Omer and Ashgriz [41] conducted evaluations of various nozzle types, including dual fluid, spiral, hydraulic, ultrasonic, rotary, and electrostatic, examining their distinct atomization modes. In the context of infrared debonding detection in CFSTs, variables such as spraying distance, atomization level, water temperature, and excitation duration during spray cooling can impact both the cooling effect and the detection outcomes. The influence of these spray-cooling parameters on infrared debonding detection during the CFST's exothermic hydration phase remains unclear. Currently, no standardized, efficient, and convenient method for spray-cooling excitation exists. Furthermore, the quantified detection of CFST debonding under cooling excitation cannot be achieved with existing infrared techniques. Thus, a comprehensive exploration of the impact of spray-cooling parameters during the exothermic hydration phase is essential for developing a foundational understanding and methodology for quantitative infrared debonding detection in CFSTs. Accordingly, a stable, efficient, and convenient spray-cooling excitation method should be formulated.

This study aims to determine the effects of various spray-cooling parameters (i.e., atomization level, spraying distance, water temperature, and excitation duration) on infrared debonding detection during the exothermic hydration of CFSTs through indoor modeling experiments. Additionally, this study explores the mechanism of surface heat transfer during cooling excitation. By integrating the principles of spray cooling with the surface heat conduction mechanism of CFSTs, this research establishes a foundation for a quantitative approach to infrared debonding detection and proposes a highly efficient and stable spray-cooling method for engineering applications. This study involved 39 sets of indoor model experiments to determine the surface temperature field distribution of CFSTs under diverse cooling excitation parameters. The average temperature difference between debonded and non-debonding regions on steel plate surfaces during excitation was used as a metric to evaluate the effectiveness of infrared detection. Subsequently, this study analyzed the variation in surface temperature difference on the steel plate throughout the

cooling excitation process, aiming to elucidate the impact of various parameters on infrared debonding detection in CFSTs.

2. Materials and Methods

2.1. Research Framework

For heating excitation, excitation duration and excitation distance are relevant parameters that need to be considered [22–27]. Similarly, for spray cooling, the temperature of the spray water and the atomization level affect the heat transfer of the steel tube, so these parameters also need to be taken into account. As shown in Figure 1, this study selects different excitation parameters (atomization level, spraying distance, tank water temperature, and excitation duration) to determine the cooling excitation conditions. Based on these conditions, spray-cooling excitation experiments are conducted, and infrared thermal imaging is employed to monitor the surface temperature of the steel plate, collecting temperature difference data throughout the excitation process, particularly the average temperature difference between debonded and non-debonded regions, which serves as a metric to evaluate the effectiveness of infrared detection. Subsequently, parametric analysis is performed to investigate the impact of excitation duration, spraying distance, and other factors on heat transfer efficiency and debonding detection accuracy. Finally, based on the analysis results, an optimal experimental method and strategy are proposed to optimize the spray-cooling excitation process, enhancing detection efficiency and stability, thereby providing theoretical support and technical guidance for the infrared debonding detection of CFSTs in practical engineering applications.
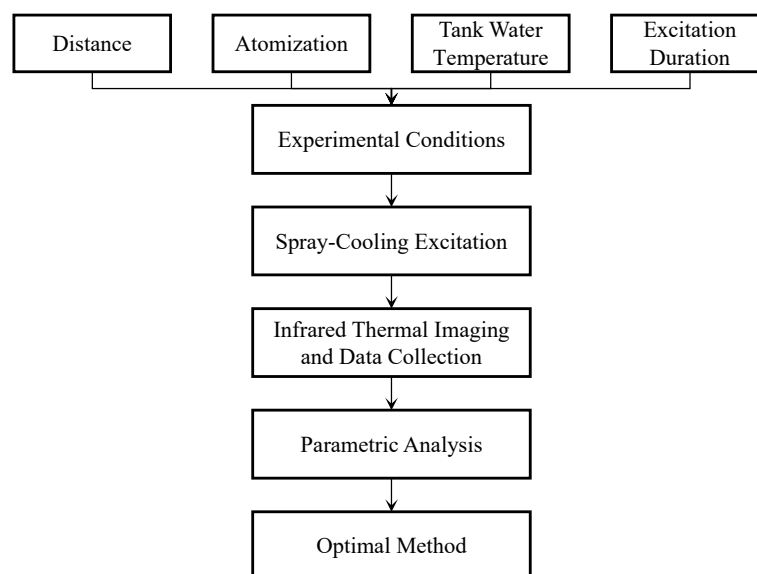

Figure 1. Research flowchart.

2.2. Spray-Cooling Excitation Method

2.2.1. Structure of the Spraying Device

This study utilizes an electric kettle equipped (Deli Electric Kettle, Deli Group Co., Ltd., Ningbo, China) with plain orifice nozzles to simulate the spray-cooling effect on the surface temperature field of a CFST during its exothermic hydration process. The specifications of the system are detailed in Table 1. Plain orifice nozzles, noted for their simplicity and widespread use, are employed in this setup (refer to Figure 2 for the structure) [41]. The temperature of the water in the tank is regulated by filling the tank with water at various temperatures.

Table 1. Specifications of spraying system.

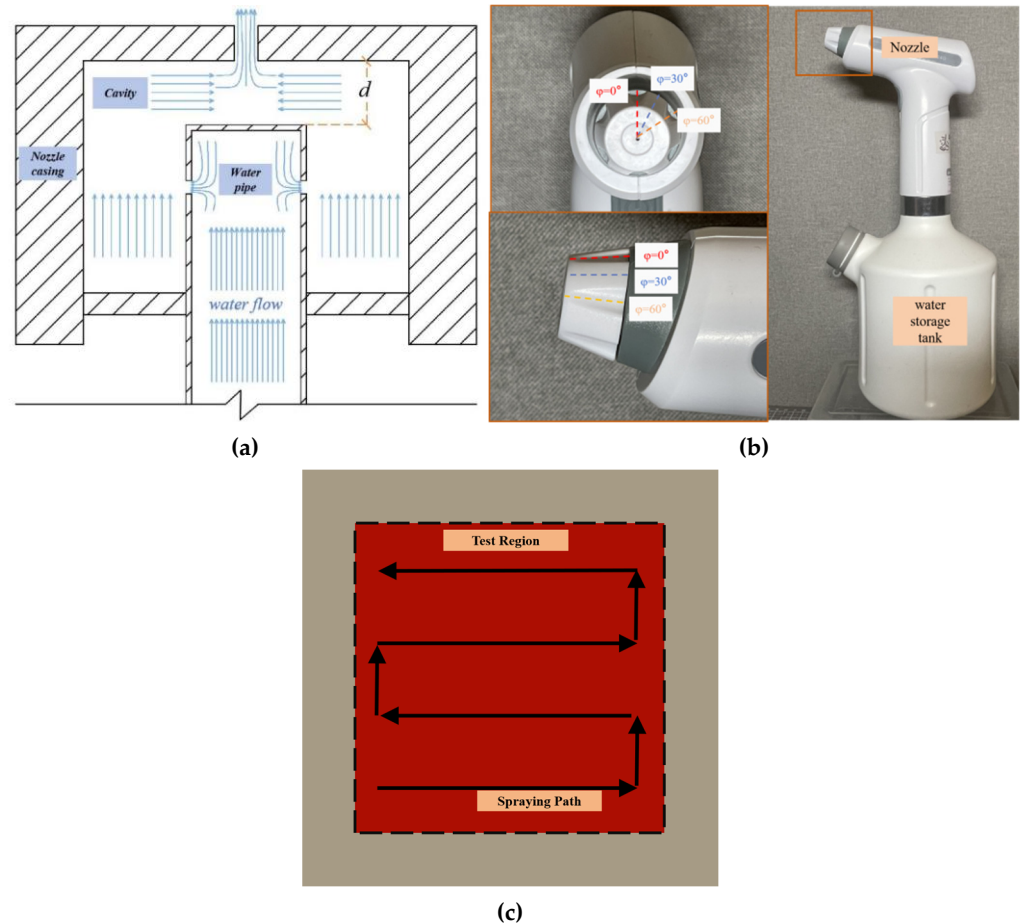| Device Model	Tank Volume	Nozzle Type
DL581040	1000 mL	Plain orifice

(a)   (b)

(c)

Figure 2. Spraying device details: (**a**) schematic layout of a plain orifice nozzle, (**b**) structure of the spraying device, and (**c**) design diagram of spraying path.

Figure 2a illustrates the nozzle structure utilized for cooling excitation in this study. The nozzle comprises an outer shell and an inner water pipe, which are screwed together to form a cavity. Water from the tank is pressurized by a pump into the nozzle pipe, passes through holes in the pipe, and is then sprayed out from apertures at the nozzle's top. The height of this cavity at the nozzle's apex (d) can be altered by adjusting the nozzle shell's angle (φ), as depicted in Figure 2b. An increase in angle φ results in a corresponding increase in height d of the cavity. According to Bernoulli's equation and the continuity equation [42], a decrease in d leads to an increase in the water's flow velocity at the nozzle outlet. Given that the outlet aperture is constant, changes in the internal cavity's water velocity affect the atomization degree of the water spray and the maximum spray distance. The Sauter mean diameter (SMD) is typically used to quantitatively assess the degree of liquid atomization [43,44]. Research indicates that as the liquid flow rate increases, the SMD of the droplets decreases, enhancing the atomization degree [45–47]. The excitation path, shown in Figure 2c, involves uniformly spraying water from the bottom to the top of the detection region at a constant speed, ensuring that the mist covers the entire test area evenly.

2.2.2. Control Parameters for Spray Excitation

As depicted in Figure 2, this study employs three different nozzle rotation angles ($\varphi = 0°$, $\varphi = 30°$, $\varphi = 60°$), corresponding to three distinct cavity heights: *dmin*, *dmid*, and *dmax* (with *dmax* > *dmid* > *dmin*). The morphology of water spray at these three cavity heights was captured using a camera (Sony ZVE-10, Sony Corporation, Japan, Tokyo), and the maximum spray distance was measured using a measuring tape (Delixi Electric Co., Ltd., Wenzhou, China).

Figure 3 shows the water spray morphology for the three nozzle rotation angles. A comparative analysis of Figure 3a–c reveals that the water forms a cone-shaped spray pattern, with the liquid ejected from all three nozzles in droplet form. Notably, the degree of atomization diminishes as the cavity height increases, a finding that aligns with previous research [46,47]. The spray distance achieved by the three nozzles extends with increasing cavity height, with the shortest distance observed for the $\varphi = 0°$ (*dmin*) nozzle (95 cm).
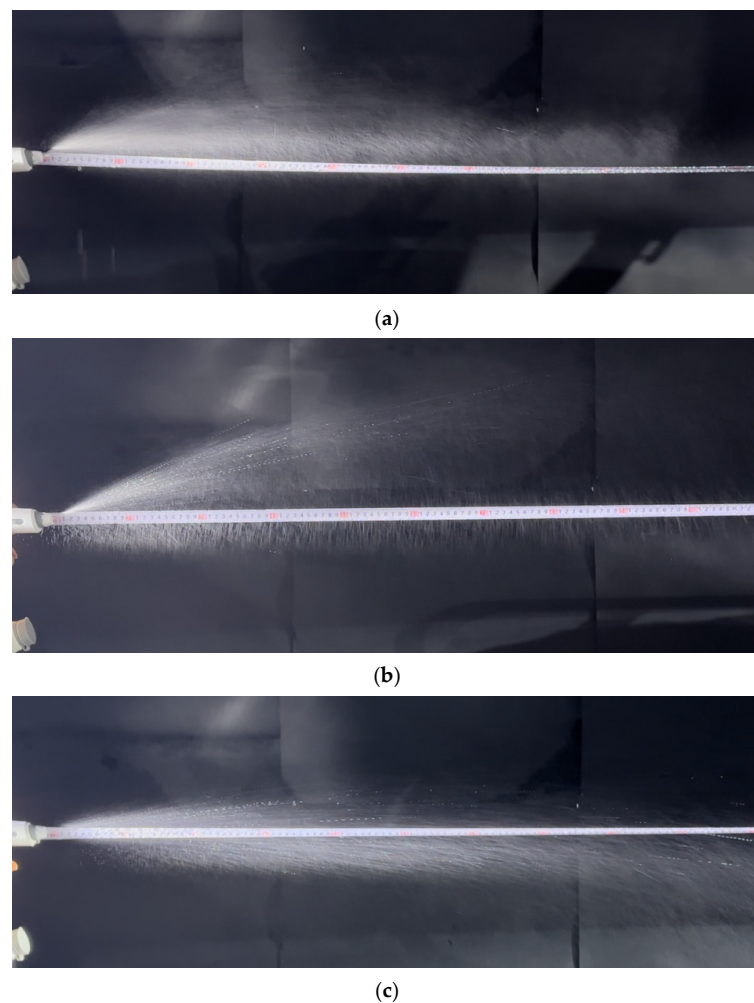

(**a**)

(**b**)

(**c**)

Figure 3. Water spray morphologies: (**a**) nozzle angle $\varphi = 0°$ and cavity height *dmin*, (**b**) nozzle angle $\varphi = 30°$ and cavity height *dmid*, and (**c**) nozzle angle $\varphi = 60°$ and cavity height *dmax*.

Table 2 outlines the relationship between nozzle rotation angles, cavity heights, and atomization levels. The atomization degree progressively declines as cavity height increases. In this study, three nozzle angles ($\varphi = 0°$, 30°, and 60°) were selected to generate three distinct cavity heights (*dmin*, *dmid*, and *dmax*), thereby defining three atomization levels: high, medium, and low. Given that the spray distance of droplets at the high atomization level is limited to 95 cm, the excitation distances used in subsequent tests in this study are set to be less than or equal to 95 cm.

Table 2. Nozzle rotation angles, cavity heights, and corresponding atomization levels.

Nozzle Rotation Angle φ	Cavity Height	Atomization Level
0°	*dmin*	High
30°	*dmid*	Medium
60°	*dmax*	Low

2.3. Experimental Study

2.3.1. Test Platform

As depicted in Figure 4a, this study designed a test platform to simulate the temperature field on the outer surface of a CFST during its exothermic hydration stage. The platform comprises a polyvinyl chloride (PVC) water tank (Hebei Feilong Plastic & Rubber Products Co., Ltd., Hebei, China), coated steel plates (Q235 steel, produced by Chongqing Iron and Steel (Group) Co., Ltd., Chongqing, China), a heating rod (SUSUN Co., Ltd., Zhejiang, China), temperature sensors (TP-100, Shanghai Anyi instruments Co., Ltd., Shanghai, China), prefabricated debonding samples (Kangtai Polymer Materials Co., Ltd., Zhuhai, China), and propellers (SUNSUN Co., Ltd., Zhejiang, China). In practical engineering, interface debonding occurs only at the contact between the concrete and the inner wall of the steel pipe. Therefore, the experiment focuses solely on simulating the temperature change at the concrete interface rather than the core area's temperature [32]. This is achieved through controlled-temperature hot water, a method validated by Yang et al. [32] for simulating concrete's heat generation. In this study, the exothermic hydration of concrete is similarly simulated using heated water. Given that CFSTs in practical engineering typically have diameters ranging from 1.4 to 1.6 m with low surface curvature, the influence of tube curvature on detection results is negligible at the close excitation distances used. For experimental convenience, rectangular steel plates are used to simulate CFSTs.
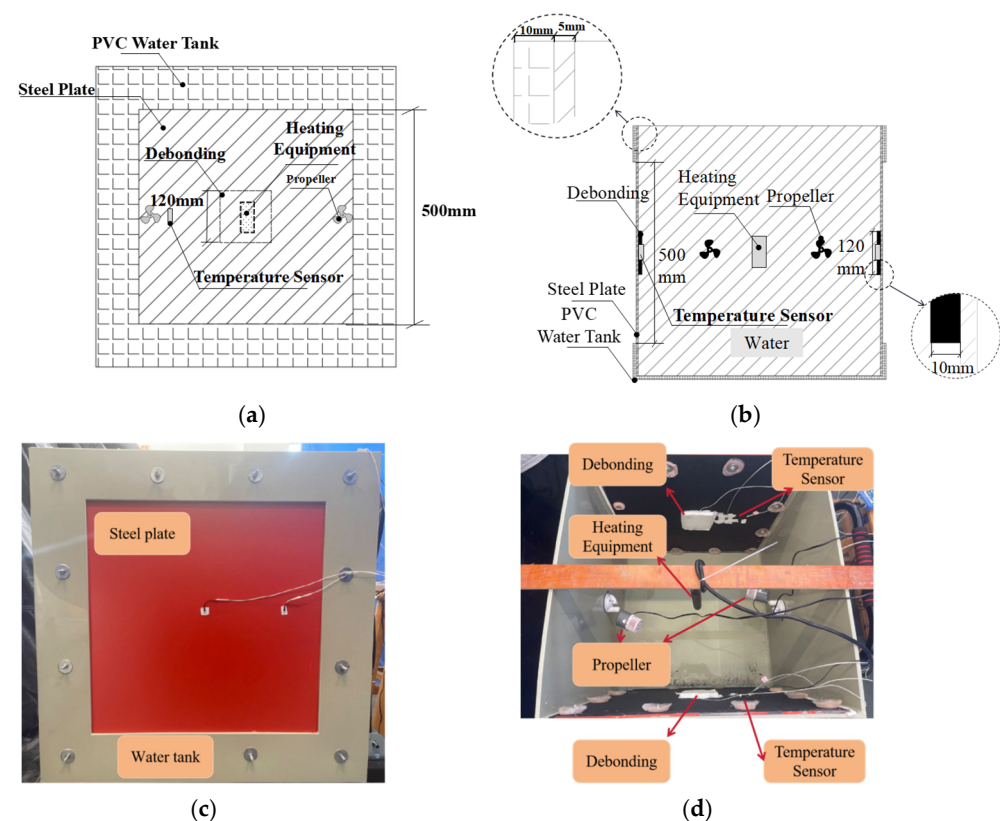

Figure 4. Test platform design and construction: (**a**) front view schematic, (**b**) side view schematic, (**c**) exterior front view, and (**d**) interior side view.

The PVC water tank, with internal dimensions of 700 mm × 700 mm × 700 mm (Figure 4b), has openings of 500 mm × 500 mm on the front and rear sides. Two steel plates (600 mm × 700 mm × 5 mm) are attached to the front and rear sides inside the tank to simulate CFST exteriors. Infrared cameras are positioned for clear views of the steel plate surfaces through these openings. The steel plates are coated with the same paint used on a CFST arch bridge in China.

Styrofoam, having thermal conductivity and specific heat capacity similar to air, is adhered to the steel plates inside the water tank to simulate debonding (Figure 4c). The prefabricated debonding voids, measuring 120 mm × 120 mm × 10 mm, are centrally located on the steel plates. To prevent water ingress into the voids, these areas are covered with cling wrap and sealed with glass adhesive. Heated water is poured into the tank to mimic concrete's exothermic hydration process. A heating rod, suspended in the tank, and temperature sensors, placed on the steel plates' inner sides, facilitate real-time temperature monitoring at the steel–water interfaces. The heating pump is activated to maintain the water temperature at a constant 55.5 °C ± 0.3 °C, reflecting the peak interface temperature during actual CFST exothermic hydration. Two propellers, mounted on the left and right sides of the tank, ensure a uniform water temperature distribution.

2.3.2. Experimental Design and Procedure

The experimental setup, as illustrated in Figure 4a,b, includes infrared cameras positioned on both the front and rear sides of the water tank. These cameras are responsible for detecting the surface temperatures of the two steel plates and capturing their temperature field data. During the experiments, the ambient conditions were controlled to maintain a stable room temperature of 29 °C with minimal airflow. Initially, water heated to 55.5 °C was poured into the tank until the steel plates were fully submerged. This water temperature was consistently maintained at 55.5 °C ± 0.3 °C using a heating pump and temperature sensors. After stabilizing the water temperature in the tank for 1 h, the cooling excitation test commenced. To optimize the experiment's duration, excitation was alternately conducted on the two steel plates. The infrared cameras recorded the temperature field data on the steel plate surfaces throughout the excitation process. The detection period encompassed the entirety of the tests under each excitation condition and continued for 1200 s after excitation. Enclosures were set up around the test platform to prevent ambient light from reflecting off the steel plate surfaces and interfering with the infrared camera readings.

The experiment investigated the impact of various water temperatures in the tank, excitation distances, excitation durations, and atomization levels on infrared debonding detection, employing the excitation method detailed in Section 2. The test conditions, as outlined in Figures 5 and 6, comprised two primary parts. The first part (Figure 6) examined the effects of different water temperatures inside the tank, excitation distances, and atomization levels on infrared detection, using a constant water volume of 500 mL for excitation. This part included excitation distances of 45, 60, 80, and 95 cm, along with water temperatures of 5.5, 10, and 28.5 °C (room temperature) and high and low atomization levels. Test conditions were labeled in the sequence of atomization level, water temperature, and excitation distance; for instance, H-5.5-45 indicates the high atomization level, a 5.5 °C water temperature, and a 45 cm excitation distance.
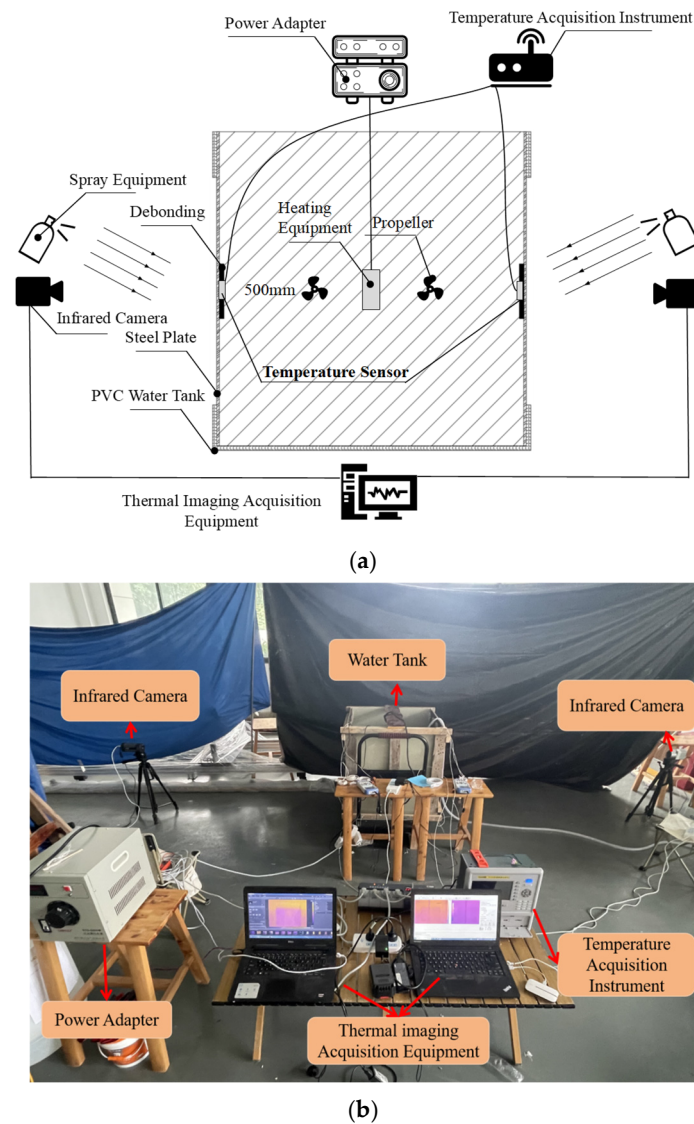
(**a**)

(**b**)

Figure 5. Experimental design and setup: (**a**) schematic and (**b**) photograph.
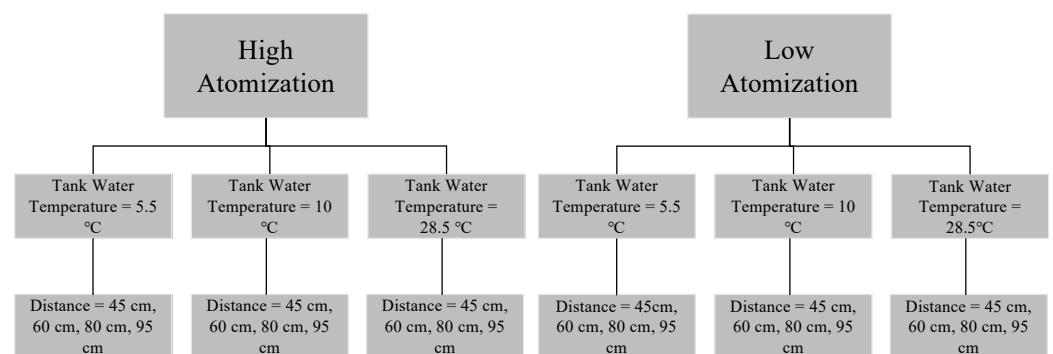

Figure 6. Set 1 of experimental conditions.

The second part of the experiment (Figure 7) focused on the effects of varying excitation durations and atomization levels on infrared detection. This part utilized excitation durations of 40, 80, 120, 200, and 350 s with high, medium, and low atomization levels while maintaining a constant water temperature of 28.5 °C (room temperature) and an excitation distance of 95 cm. Test conditions were labeled according to atomization level and excitation duration; for example, H-40s denotes the high atomization level with a 40 s excitation duration. To avoid interference between consecutive sets of conditions, a

1200 s interval was allotted following the completion of tests for each group. The water temperature inside the tank was verified using a thermometer (alcohol thermometer, accuracy ±0.1 °C, Shanghai Anyi Instruments Co., Ltd., Shanghai, China) before each cooling excitation to ensure compliance with the experimental requirements.
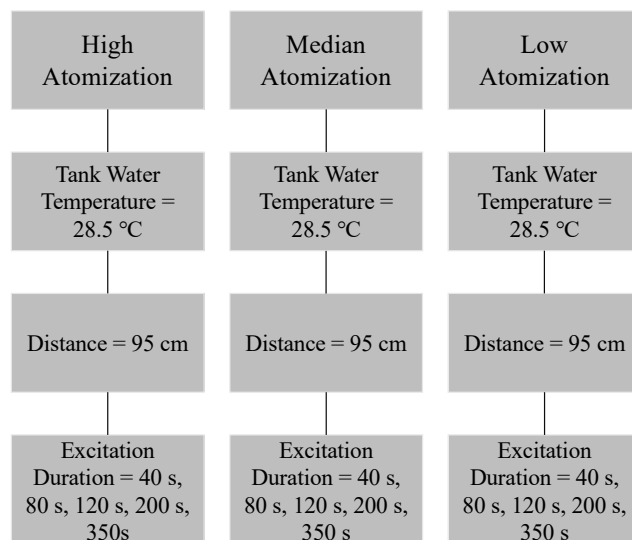
High Atomization	Median Atomization	Low Atomization
Tank Water Temperature = 28.5 °C	Tank Water Temperature = 28.5 °C	Tank Water Temperature = 28.5 °C
Distance = 95 cm	Distance = 95 cm	Distance = 95 cm
Excitation Duration = 40 s, 80 s, 120 s, 200 s, 350s	Excitation Duration = 40 s, 80 s, 120 s, 200 s, 350 s	Excitation Duration = 40 s, 80 s, 120 s, 200 s, 350 s

Figure 7. Set 2 of experimental conditions.

2.3.3. Infrared Thermal Imaging and Data Collection

To evaluate the effectiveness of infrared thermography in detecting debonding in CFSTs under cooling excitation, the steel plate area was monitored using long-wave thermal imaging cameras. Figure 8 shows the two infrared cameras used in the experiment: the FLIR A300 (Teledyne FLIR LLC, Goleta, CA, USA) and the MGS-F6 (Shanghai Magnity Technologies Co., Ltd., Shanghai, China). The specifications of these cameras are detailed in Table 3.

(**a**)   (**b**)

Figure 8. Infrared imaging setup: (**a**) FLIR A300; (**b**) MGS-F6.

Table 3. Parameters of infrared thermal imaging cameras.

Camera Model	FLIR A300	MGS-F6
Detector type	Uncooled microbolometer	Uncooled microbolometer
NETD	<0.05 °C	<0.05 °C
Accuracy	±2 °C or ±2%	±0.7 °C or 0.7%
Resolution	320 × 240 pixels	640 × 480 pixels
Spectral range	7.5–13 μm	8–14 μm
Field of view	25° × 18.8°	25° × 19°

Both cameras are noncooled, long-wave infrared models. The FLIR A300 features a resolution of 320 × 240 pixels, a spectral range of 7.5–13 μm, and a noise equivalent temperature difference (NETD) below 0.05 °C (NETD is a metric used in infrared and thermal imaging systems to measure the device's sensitivity in detecting minor temperature variations). The MGS-F6 camera offers a higher resolution of 640 × 480 pixels, a spectral range of 8–14 μm, and an NETD below 0.05 °C. Both infrared cameras were positioned at the front and rear sides of the specimens. This setup ensured that the center of the infrared image aligned with the center of the steel plate, and the plane of the steel plate was parallel to the imaging plane of the camera. The image capture frequency for both cameras was set at one frame per second.

2.3.4. Data Analysis and Evaluation Indices

The temperature difference between the debonded and non-debonding regions serves as a critical index for evaluating the efficacy of infrared detection. Figure 9 illustrates the extraction of temperature fields from both the debonding region (T_{D}) and the non-debonding region (T_{non}) in thermal images. The relevant symbol abbreviations used in this study will be summarized in Appendix A.
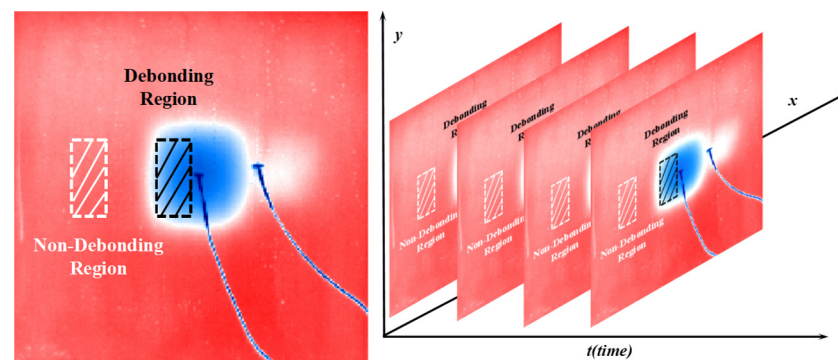

Figure 9. Temperature field extraction from debonded and non-debonding regions.

This study does not include an analysis of data from heat flux sensors affixed to the external surface of the steel plate (as shown in Figure 8). To mitigate the influence of these sensors, the left side of the steel plate's external surface was designated as the debonding region. The adjacent left part of the steel plate surface was selected as the non-debonding region. For a quantitative analysis of the impact of cooling excitation on detection effectiveness under different conditions, the following equation was employed to calculate the average temperature fields of both regions:

$$T_{\mathrm{Dmean}} = \frac{\sum\limits_{i=1}^{n} T_{\mathrm{D}i}}{n} \tag{1}$$
$$T_{\mathrm{nonmean}} = \frac{\sum\limits_{i=1}^{n} T_{\mathrm{non}i}}{n}$$

where $T_{\mathrm{D}i}$ and $T_{\mathrm{non}i}$ represent the temperatures of pixel i in the debonded and non-debonding regions, respectively. The variable n denotes the number of pixels in the selected area of the thermal images. T_{Dmean} and T_{nonmean} indicate the average temperatures of the debonded and non-debonding regions, respectively.

The average temperature difference between these regions, ΔT, is calculated using the absolute value of their difference, as follows [34]:

$$\Delta T = |T_{\mathrm{Dmean}} - T_{\mathrm{nonmean}}| \tag{2}$$

By extracting the temperature field data from each frame throughout the excitation process, as depicted in Figure 9, the average temperature difference for the entire excitation period can be obtained. An increase in the average temperature difference indicates improved resolution between the debonded and non-debonding regions. The value of ΔT under cooling excitation reflects the performance of infrared debonding detection. Furthermore, the maximum value of ΔT during the excitation period, maxΔT, is extracted as follows:

$$\max\Delta T \;=\; \max(\Delta T_1, \Delta T_2, \Delta T_3 \dots \Delta T_n) \tag{3}$$

By analyzing the timing and magnitude of maxΔT, the optimal detection moment for a single condition and the degree of detection enhancement resulting from excitation can be effectively characterized. The time at which maxΔT occurs, denoted as $t_{\max\Delta T}$, is defined as the moment when the contrast between the debonding and non-debonding areas is at its peak (the optimal detection moment). An analysis of $t_{\max\Delta T}$ facilitates the determination of the best detection time.

3. Results and Discussion

3.1. Evolution of the Average Temperature Difference During Spray-Cooling Excitation

The temporal changes in the average temperature difference under cooling excitation reflect the overall trends observed in infrared detection. Figure 10 illustrates the evolution of the average temperature difference (ΔT) under (a) different excitation distances with fixed spray-cooling water volumes and (b) varying excitation durations. Due to space limitations, the figure selectively presents representative conditions from the experiment. However, the temperature difference exhibited similar patterns across other conditions.
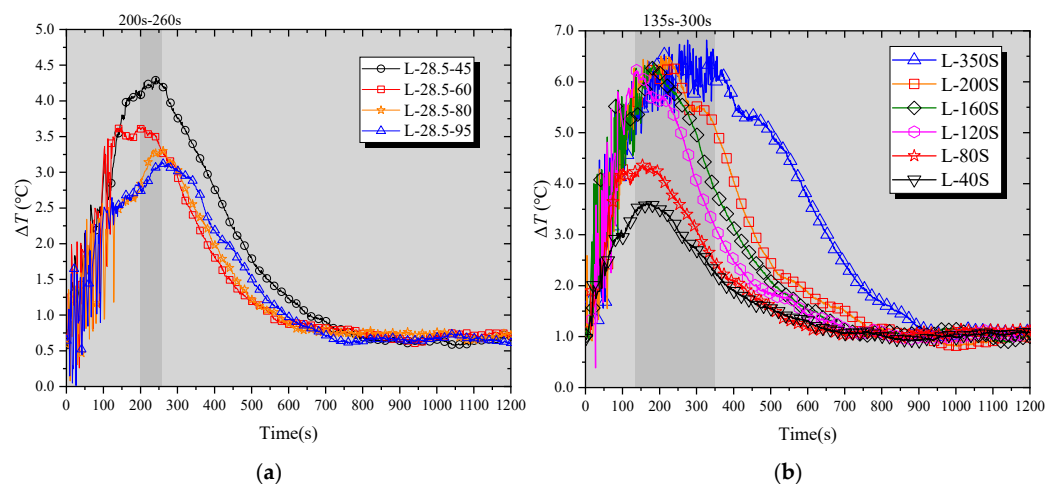

Figure 10. Temporal evolution of average temperature difference under cooling excitation: (**a**) for different excitation distances at constant water volume; (**b**) at various excitation durations.

In Figure 10a, the data demonstrate the relationship between excitation distance (45, 60, 80, and 95 cm) and the average temperature difference over time. For each condition shown, the water temperature in the tank was maintained at 28.5 °C, the total water volume of spray cooling was 500 mL, and the atomization level was selected as low. The figure indicates that the maximum average temperature difference is reached at a specific moment (approximately between 200 and 260 s), irrespective of the excitation distance. As the excitation distance increases (from 45 cm to 95 cm), the peak value of the average temperature difference progressively decreases. Approximately 750 s after the start of excitation, the value of the maximum average temperature difference for each condition reverts to the pre-cooling excitation level (around 0.75 °C).

Figure 10b presents results for conditions with a water temperature of 28.5 °C in the tank, an excitation distance of 95 cm, and a low atomization level for excitation durations ranging from 40 s to 350 s. These data show that the maximum average temperature difference increases with longer excitation durations. The average temperature difference for each condition returns to the pre-cooling excitation level approximately between 750 and 1000 s from the start of excitation. Given that experimental intervals of 1200 s (exceeding 900 s) were established between each group in this study, it can be concluded that the different experimental conditions are independent and do not influence each other.

3.2. Maximum Average Temperature Difference Relative to Excitation Distance and Water Temperature

Given that the average temperature under cooling excitation exhibits a rising and then declining trend, a maximum average temperature difference (maxΔT) value is present for each operating condition. This maxΔT value is indicative of the upper detection limit of infrared technology under cooling excitation. Both the spray distance and the water temperature within the tank significantly influence the maxΔT value. Consequently, Figure 11 plots the maxΔT values for three different tank water temperatures (5, 10, and 28.5 °C) against the excitation distance.
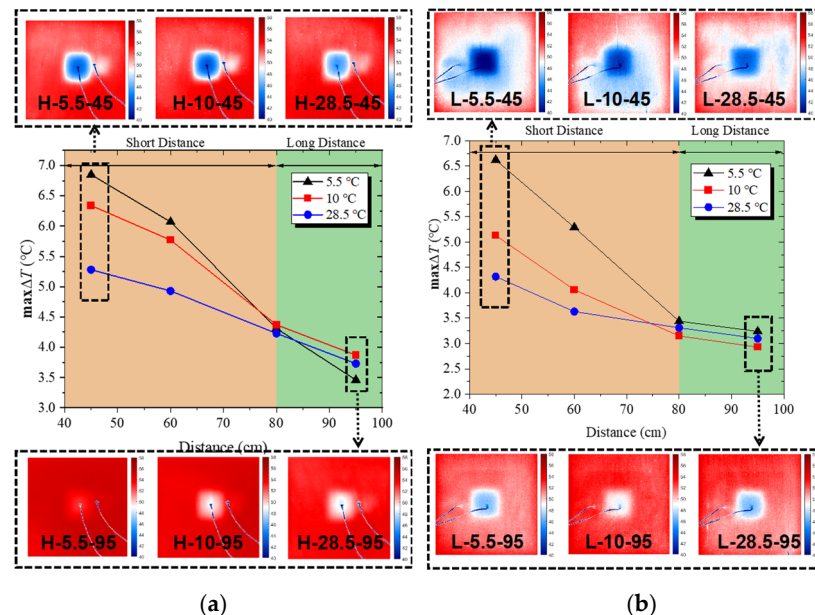

Figure 11. Maximum average temperature difference according to excitation distance at a (**a**) high atomization level and (**b**) low atomization level.

Figure 11 shows the maxΔT in relation to various spraying distances and atomization levels (high and low), along with infrared images captured at the moment when maxΔT values are observed. A noticeable low-temperature region, resembling the debonding area, is visible in the center of the infrared images, particularly for excitation distances of 45 and 95 cm. This feature aids in distinguishing the debonding. In the infrared image with a 45 cm excitation distance, the debonding region is more distinctly discernible due to a higher maxΔT compared to other excitation distances.

As shown in Figure 11a,b, when the water temperature in the tank is constant, the maxΔT decreases with an increase in excitation distance. Examining the blue curves (representing a water temperature of 28.5 °C) in Figure 11a,b, the decline in maxΔT is more pronounced at a high atomization level as the distance increases. Figure 11b demonstrates that the influence of distance on maxΔT is relatively minor when the spraying distance

ranges between 80 and 95 cm. As shown in Table 4, the standard deviations of maxΔT at three different water temperatures are 0.06 and 0.17, respectively. At the high atomization level (Figure 11a), smaller droplet volumes and decreased momentum may render the droplets more susceptible to gravitational and air disturbances during flight. This leads to fewer droplets reaching the steel plate surface as distance increases, thus diminishing the excitation effect. In contrast, at the low atomization level (Figure 11b), the droplets are larger and possess greater initial kinetic energy, resulting in a less pronounced decrease in the number of droplets reaching the test surface with increasing distance. Furthermore, the decline in maxΔT with increasing excitation distance is less severe. The maxΔT remains relatively stable when the distance is between 80 and 95 cm. As shown in Table 5, the standard deviations of maxΔT at three different water temperatures are 0.12 and 0.13, respectively.

Table 4. Maximum average temperature difference according to excitation distance at a high atomization level.

Distance	5.5 °C	10 °C	28.5 °C	Standard Deviation
45 cm	6.85 °C	6.34 °C	5.28 °C	0.65 °C
60 cm	6.07 °C	5.77 °C	4.93 °C	0.48 °C
80 cm	4.31 °C	4.37 °C	4.23 °C	0.06 °C
95 cm	3.46 °C	3.87 °C	3.73 °C	0.17 °C

Table 5. Maximum average temperature difference according to excitation distance at a low atomization level.

Distance	5.5 °C	10 °C	28.5 °C	Standard Deviation
45 cm	6.62 °C	5.13 °C	4.32 °C	0.95
60 cm	5.29 °C	4.06 °C	3.63 °C	0.70
80 cm	3.44 °C	3.15 °C	3.31 °C	0.12
95 cm	3.24 °C	2.93 °C	3.1 °C	0.13

Figure 11a indicates that at distances below 80 cm (marked as the orange background) and with a constant excitation distance, a lower water temperature in the tank leads to an increased maximum average temperature difference. When the distance is 80 cm or greater (denoted as the green background), the maxΔT values for the three tested water temperatures (5.5, 10, and 28.5 °C) exhibit minimal variation (standard deviation of maxΔT ≤ 0.17), suggesting that the water temperature in the tank has a negligible effect on the maxΔT at these distances. A similar trend is observed in Figure 11b; for distances of 80 cm or more (green background), the maxΔT values across the three water temperatures are comparatively uniform (standard deviation of maxΔT ≤ 0.13), indicating a minimal impact of water temperature on maxΔT. This pattern can be attributed to the heat exchange between the droplets and the air during their flight. As droplets travel, they gradually warm up due to this exchange [44]. At shorter spraying distances (<80 cm), the flight duration of the droplets is limited, providing insufficient time for them to absorb significant ambient heat before reaching the steel plate. In such cases, the water temperature in the tank considerably influences the maxΔT. At longer distances ($\geq$80 cm), the droplets experience more prolonged heating in the air, often reaching temperatures close to room temperature (28.5 °C) by the time they contact the steel plate. Under these conditions, the initial water temperature has almost no impact on the maxΔT.

In summary, under cooling excitation, the maxΔT between the debonded and non-debonding regions is significantly enhanced, ranging from 3 °C to 7 °C. Particularly at the low atomization level, when the spraying distance extends to 80–90 cm, the maxΔT

shows insensitivity to both the spraying distance and the water temperature in the tank. During this phase, the maxΔT (ranging from 3.1 °C to 3.4 °C) remains relatively stable. This temperature differential is substantial enough to effectively distinguish debonding areas.

3.3. Timing of the Maximum Average Temperature Difference Relative to the Excitation Duration

The timing of the maximum average temperature difference determines the optimal detection moment, and conducting the detection at this moment helps improve accuracy. Figure 12 and Table 6 illustrate the timing of the maximum average temperature difference ($t_{\max\Delta T}$) in relation to the excitation duration at various atomization levels. The duration of spray-cooling excitation affects the total heat exchange between the steel plate and water, consequently influencing the average temperature difference between the debonded and non-debonding regions. The dashed line in Figure 12 indicates that the occurrence of the maxΔT aligns with the duration of the excitation. However, the timing of maxΔT following spray-cooling excitation does not exhibit a direct linear correlation with the excitation duration. For excitation durations shorter than 120 s (marked as the green background in Figure 11) and at a consistent atomization level, the correlation between the timing of maxΔT and the excitation duration appears relatively weak. The moments of occurrence are clustered within a narrow range: from 135 s to 175 s at the low atomization level, from 95 s to 135 s at the medium level, and from 125 s to 165 s at the high atomization level. Conversely, when the excitation duration exceeds 120 s (indicated by the blue background) at the same atomization level, the timing of maxΔT tends to increase proportionally with the excitation duration. In this phase, the occurrence of maxΔT for both low and medium atomization levels closely approaches the conclusion of the excitation period.
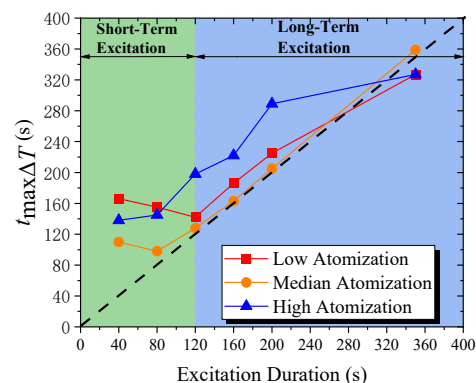

Figure 12. Temporal relation of average temperature difference to excitation duration.

Table 6. The timing of the maximum temperature difference under different excitation durations and atomization levels.

Excitation Duration (s)	Low Atomization	Median Atomization	High Atomization
40	166 s	110 s	138 s
80	155 s	98 s	145 s
120	142 s	128 s	198 s
160	186 s	163 s	222 s
200	225 s	205 s	289 s
350	327 s	359 s	327 s

Figure 13 illustrates the liquid morphologies on the steel plate surface at different excitation durations for the medium atomization level test group. In this study, the surface

temperature of the steel plate in the specimen was maintained at 55.5 °C $\pm$ 0.3 °C, a temperature insufficient to induce boiling of the liquid droplets. The heat exchange between the liquid droplets and the steel plate primarily occurs through surface evaporation and forced convection resulting from the impact of heated surface droplets [31]. As shown in Figure 13, at an excitation duration of 40 s, the water on the steel plate surface predominantly exists as liquid droplets with limited mobility. With increasing excitation duration (from 40 s to 120 s), these droplets gradually coalesce and flow under the influence of gravity. Further extension of the excitation time (from 120 s to 350 s) leads to a noticeable downward flow of water on the steel plate surface. When the excitation duration is short (<120 s), the limited time and water volume prevent the formation of a fast-flowing water stream on the steel plate. Under these conditions, heat dissipation from the steel plate surface primarily occurs through evaporation. After excitation ceases, evaporation continues to contribute to heat transfer, further increasing the maximum average temperature difference. As the liquid gradually evaporates, the efficiency of heat transfer by evaporation decreases, leading to the peak in maxΔT. Consequently, a weak correlation is observed between the excitation duration and the timing of maxΔT. However, for longer excitation durations (>120 s), the continuous water flow on the steel plate surface effectively removes heat, primarily through forced convection. Once the excitation stops, this dominant convection rapidly diminishes, making it challenging to further expand the temperature difference between the debonded and non-debonding regions. This results in the temperature peak being reached sooner. Therefore, a more pronounced linear correlation is observed between the excitation duration and the timing of the maximum temperature difference.
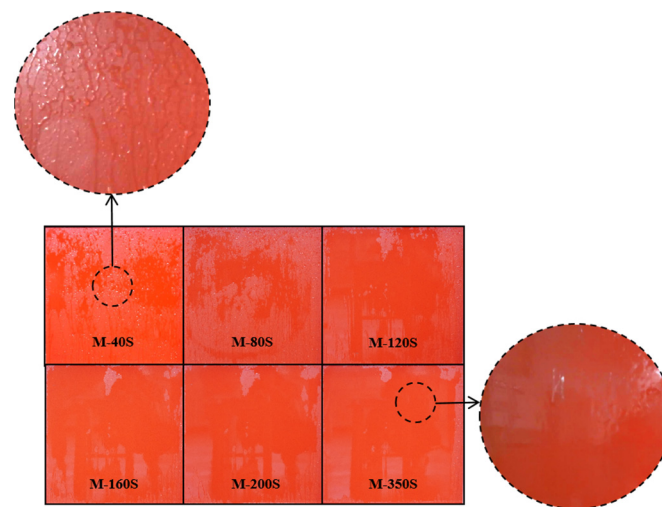

Figure 13. Liquid morphology on steel plate surface at medium atomization level over various excitation durations.

In summary, different excitation durations lead to variations in the water morphology on the steel plate, resulting in two distinct modes of heat exchange. This variation in heat exchange mechanisms may explain why the timing of the appearance of the maxΔT following spray-cooling excitation does not exhibit a strict linear correlation with the excitation duration.

3.4. Maximum Average Temperature Difference Relative to Excitation Duration

In practical detection, the larger the maxΔT, the more favorable it is for detection. Figure 14 and Table 7 present the maximum average temperature difference in relation to the excitation duration under various working conditions. When the excitation duration is short (<120 s, indicated as the green region), there is only a marginal difference in maxΔT

across the three atomization levels at the same excitation duration. This suggests a weak correlation between maxΔT and atomization level, implying that maxΔT is predominantly influenced by the excitation duration. Experimental results across the three atomization levels indicate a consistent increase in maxΔT corresponding to longer excitation durations. In cases where the excitation duration is extended (≥ 120 s, labeled as the blue region), maxΔT decreases with an increase in atomization level under the same excitation time. At a constant atomization level, maxΔT exhibits a gradual increase with longer excitation durations, tending to stabilize around a nearly constant value. Under long excitation durations (≥ 120 s), heat exchange on the steel plate surface is primarily dominated by forced convection. Due to the larger volume of liquid droplets at the low atomization level, the heat transfer on the steel plate surface is more intense compared to the high atomization level test group, leading to a more significant increase in maxΔT for the low atomization level group.
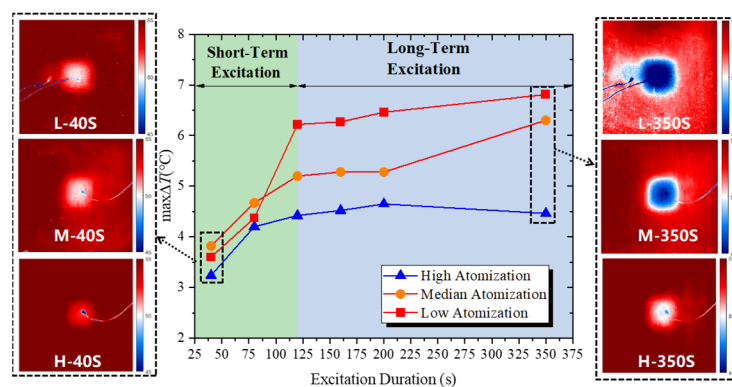

Figure 14. Maximum average temperature difference by excitation duration.

Table 7. Maximum average temperature difference by excitation duration.

Excitation Duration (s)	Low Atomization	Median Atomization	High Atomization
40	3.6 °C	3.82 °C	3.24 °C
80	4.37 °C	4.67 °C	4.2 °C
120	6.22 °C	5.2 °C	4.42 °C
160	6.27 °C	5.28 °C	4.52 °C
200	6.46 °C	5.28 °C	4.65 °C
350	6.81 °C	6.3 °C	4.46 °C

In summary, under consistent atomization levels and extended excitation durations, there is minimal variation in maxΔT relative to the excitation duration. Specifically, when long durations (≥ 120 s), low atomization levels, and extended distances (≥ 80 cm) are selected for spray-cooling excitation, the variation in maxΔT after excitation is minor (with a standard deviation of 0.23 °C). Under these conditions, maxΔT typically occurs close to the end of the excitation period, and its value shows limited correlation with the selection of various excitation parameters. Instead, the value of maxΔT may be more related to factors such as the debonding shape, CFST structure, material properties, and peak concrete temperature. Additionally, the range of maxΔT achieved under these conditions (between 6.22 and 6.81 °C), compared to the ΔT before cooling excitation (approximately 1 °C), increases by about five times, which is sufficient to detect the presence of debonding in typical scenarios. In practical detection, the detection personnel can use the above method to actively excite the CFST test area, without needing to control the water temperature during excitation. It is sufficient to let the water temperature approach ambient temperature.

After excitation, infrared images can be immediately collected to identify the debonding. Compared to traditional thermal excitation methods, such as microwave heating (900 W equipment power) [22] and flashlamp heating (single bulb power of 250 W) [25] the cooling excitation method proposed in this paper can be implemented while the object is in the exothermic phase, without requiring additional energy sources for excitation, making it a simpler and more suitable method for outdoor use.

4. Conclusions

The application of spray-cooling excitation significantly enhances the maximum average temperature difference between debonded and non-debonding regions, thereby improving the efficacy of infrared thermography for detecting debonding in CFSTs. Specifically, under the conditions of a low atomization level and extended spraying distance, the impact of both the spraying distance and the water temperature within the tank on the maximum average temperature difference is minimal.

When the spraying duration is short, the primary mode of heat removal from the steel plate surface is through surface evaporation. In such scenarios, the maximum average temperature difference occurs within a specific range and tends to increase with the duration of excitation. With prolonged excitation, the dominant mechanism for heat removal shifts to forced convective flow. Consequently, the variation in the maximum average temperature difference in response to the excitation duration becomes relatively minor.

We studied spray-cooling excitation with a long duration ($\geq$120 s), low atomization level, and extended distance ($\geq$80 cm). In this context, spray-cooling excitation significantly increases the maximum average temperature difference, and variations in the spray-cooling parameters have only a minor effect on this temperature difference. Additionally, the optimal moment for detection typically aligns with the end of the excitation period.

In practical testing, an excitation duration greater than 120 s, an excitation distance greater than 80 cm, and an excitation water temperature set to ambient temperature with a low atomization level can be selected. This method can increase the maximum average temperature difference by about five times compared to before excitation, without the need for additional manual control of the excitation water temperature, making it convenient for application in actual engineering. The use of water as the excitation source avoids environmental pollution and is cost-effective. Additionally, no extra energy supply equipment is required, which helps reduce project costs and improve project efficiency.

5. Limitations and Future Work

However, it is important to note that this study is limited to laboratory experiments and has not been applied in real-world engineering settings. The findings and methods presented here may not fully account for the complexities and variables present in actual engineering environments, and further validation in practical engineering projects is necessary to assess the method's performance and reliability under real-world conditions. Future research should consider adopting the method of spray-cooling excitation to minimize research variables, enabling a more focused and controlled investigation. This approach is expected to facilitate a comprehensive examination of how additional factors—such as CFST (concrete-filled steel tube) dimensions, debonding sizes, and the temperature of exothermic hydration—affect the maximum average temperature difference. A deeper understanding of these factors could lead to the more precise and quantitative detection of debonding, providing valuable insights for both theoretical and practical applications. Furthermore, exploring the development of highly mobile spray-cooling equipment would allow for the more efficient utilization of excitation water, enabling precise targeting and uniform cooling. This innovation would enhance detection efficiency by reducing water

waste and energy consumption. Ultimately, the integration of such advanced equipment into engineering practices promises not only more efficient, stable, and convenient detection of debonding but also a more sustainable approach for large-scale industrial applications.

Author Contributions: H.C.: Conceptualization, Writing—Original Draft, Review and Editing, Data Curation, Formal Analysis, Validation. C.C.: Methodology, Writing—Review and Editing, Project Administration, Funding Acquisition. All authors have read and agreed to the published version of the manuscript.

Data Availability Statement: The original contributions presented in this study are included in this article. Further inquiries can be directed to the corresponding authors.

Conflicts of Interest: The authors declare no conflicts of interest.

Appendix A

T_{Dmean}: Average temperatures of the debonded regions;

$T_{nonmean}$: Average temperatures of the non-debonded regions;

ΔT: The average temperature difference between non-debonded regions and debonded regions;

$\max\Delta T$: The maximum value of ΔT during the excitation period;

$t_{\max\Delta T}$: The timing of the maximum average temperature difference.

References

1. Han, L.-H.; Li, W.; Bjorhovde, R. Developments and advanced applications of concrete-filled steel tubular (CFST) structures: Members. *J. Constr. Steel Res.* **2014**, *100*, 211–228. [CrossRef]
2. Chen, B.-C.; Wang, T.-L. Overview of Concrete Filled Steel Tube Arch Bridges in China. *Pract. Period. Struct. Des. Constr.* **2009**, *14*, 70–80. [CrossRef]
3. Zhu, Y.; Yang, H.; Yang, X.; Sun, F. Behavior of concrete-filled steel tubes subjected to axial impact loading. *J. Constr. Steel Res.* **2020**, *173*, 106245. [CrossRef]
4. Ou, Z.; Chen, B.; Hsieh, K.H.; Halling, M.W.; Barr, P.J. Experimental and Analytical Investigation of Concrete Filled Steel Tubular Columns. *J. Struct. Eng.* **2011**, *137*, 635–645. [CrossRef]
5. Liao, F.-Y.; Han, L.-H.; He, S.-H. Behavior of CFST short column and beam with initial concrete imperfection: Experiments. *J. Constr. Steel Res.* **2011**, *67*, 1922–1935. [CrossRef]
6. Xue, J.-Q.; Fiore, A.; Liu, Z.-H.; Briseghella, B.; Marano, G.C. Prediction of ultimate load capacities of CFST columns with debonding by EPR. *Thin-Walled Struct.* **2021**, *164*, 107912. [CrossRef]
7. Xue, J.-Q.; Briseghella, B.; Chen, B.-C. Effects of debonding on circular CFST stub columns. *J. Constr. Steel Res.* **2012**, *69*, 64–76. [CrossRef]
8. Han, L.-H.; Ye, Y.; Liao, F.-Y. Effects of Core Concrete Initial Imperfection on Performance of Eccentrically Loaded CFST Columns. *J. Struct. Eng.* **2016**, *142*, 04016132. [CrossRef]
9. Shi-Cong, Y.; Fu-Min, W.; Ping, Q.U. Brief Introduction to the Core Concrete's Empty Influence on the Mechanical Performance of Concrete Filled Steel Tube Components. *J. Chongqing Jiaotong Univ.* **2008**, *27*, 360–365.
10. Lu, Z.; Guo, C.; Li, G. Air void and ring gap effect on CFST arch bridges dynamic performance. *J. Constr. Steel Res.* **2021**, *177*, 106418. [CrossRef]

11. Zhang, Z.; Pang, K.; Xu, L.; Zou, Y.; Yang, J.; Wang, C. The bond properties between UHPC and stone under different interface treatment methods. *Constr. Build. Mater.* **2023**, *365*, 130092. [CrossRef]

12. Wen, Y.N.; Su, J.C. Overview of Concrete Filled Steel Tube Viod Countermeasures. *Appl. Mech. Mater.* **2013**, *256–259*, 1121–1124. [CrossRef]

13. Chen, X.; Liao, F.; Mohamed, H.S.; Wang, J.; Huang, Z.; Zhang, K. Behavior of CFRP strengthened concrete-filled steel tubes with spherical-cap gap under axial compression. *Structures* **2023**, *58*, 105339. [CrossRef]

14. Ciampa, F.; Mahmoodi, P.; Pinto, F.; Meo, M. Recent Advances in Active Infrared Thermography for Non-Destructive Testing of Aerospace Components. *Sensors* **2018**, *18*, 609. [CrossRef]

15. Clark, M.R.; McCann, D.M.; Forde, M.C. Application of infrared thermography to the non-destructive testing of concrete and masonry bridges. *NDT E Int.* **2003**, *36*, 265–275. [CrossRef]

16. Tang, Q.; Dai, J.; Bu, C.; Qi, L.; Li, D. Experimental study on debonding defects detection in thermal barrier coating structure using infrared lock-in thermographic technique. *Appl. Therm. Eng.* **2016**, *107*, 463–468. [CrossRef]

17. Iyer, S.; Sinha, S.K.; Tittmann, B.R.; Pedrick, M.K. Ultrasonic signal processing methods for detection of defects in concrete pipes. *Autom. Constr.* **2012**, *22*, 135–148. [CrossRef]

18. Hola, J.; Sadowski, L.; Schabowicz, K. Nondestructive identification of delaminations in concrete floor toppings with acoustic methods. *Autom. Constr.* **2011**, *20*, 799–807. [CrossRef]

19. Shen, W.; Bai, H.; Wang, F.; Li, C.; Du, F. Acoustic Emission characteristics and damage evolution of Concrete-Encased CFST columns under compressive load. *Eng. Fract. Mech.* **2024**, *311*, 110578. [CrossRef]

20. Shao, Z.; Zha, X. Research on detection of gap defect of CFST based on temperature method. *Structures* **2024**, *61*, 105977. [CrossRef]

21. Cheng, C.; Chen, D.; Shao, S.; Na, R.; Cai, H.; Zhou, H.; Wu, B. Revealing the Impact of Depth and Surface Property Variations on Infrared Detection of Delamination in Concrete Structures Under Natural Environmental Conditions. *Buildings* **2025**, *15*, 10. [CrossRef]

22. Cuccurullo, G.; Berardi, P.G.; Carfagna, R.; Pierro, V. IR temperature measurements in microwave heating. *Infrared Phys. Technol.* **2002**, *43*, 145–150. [CrossRef]

23. Fang, W.; Yang, X.; Wang, X.; Hu, G.; Tao, N.; Zhang, C. Sequential laser pulse thermal excitation method for the detection of defects in metallic materials. In Proceedings of the Infrared, Millimeter-Wave, and Terahertz Technologies VIII 2021, Nantong, China, 10–12 October 2021. [CrossRef]

24. Xu, Y.; Sohn, H. Nondestructive debonding detection of fiber reinforced plastics strengthened structure based on infrared thermal imaging with laser thermal excitation. In Proceedings of the Sensors and Smart Structures Technologies for Civil, Mechanical, and Aerospace Systems 2020, Online, 27 April–9 May 2020; pp. 128–144. [CrossRef]

25. Deane, S.; Avdelidis, N.P.; Ibarra-Castanedo, C.; Williamson, A.A.; Withers, S.; Zolotas, A.; Maldague, X.P.V.; Ahmadi, M.; Pant, S.; Genest, M.; et al. Development of a thermal excitation source used in an active thermographic UAV platform. *Quant. InfraRed Thermogr. J.* **2022**, *20*, 198–229. [CrossRef]

26. Li, D.; Yang, H.; Qin, Q. Optimal design of flash thermal excitation in infrared nondestructive testing system. In Proceedings of the 3rd IEEE International Conference on Electronic Information Technology and Computer Engineering, EITCE 2019, Xiamen, China, 18–20 October 2019; pp. 1771–1775. [CrossRef]

27. Zhang, Q.; Liu, J.; Gu, J.; Tian, Y. Study on coal-rock interface characteristics change law and recognition based on active thermal excitation. *Eur. J. Remote Sens.* **2022**, *55*, 35–45. [CrossRef]

28. Tang, Q.; Liu, J.; Dai, J.; Yu, Z. Theoretical and experimental study on thermal barrier coating (TBC) uneven thickness detection using pulsed infrared thermography technology. *Appl. Therm. Eng.* **2017**, *114*, 770–775. [CrossRef]

29. Bu, C.; Tang, Q.; Liu, Y.; Yu, F.; Mei, C.; Zhao, Y. Quantitative detection of thermal barrier coating thickness based on simulated annealing algorithm using pulsed infrared thermography technology. *Appl. Therm. Eng.* **2016**, *99*, 751–755. [CrossRef]

30. Sun, J.; Xie, J. Simulation analysis of the hydration heat of large diameter CFST arch and its effects on loading age. *Appl. Therm. Eng.* **2019**, *150*, 482–491. [CrossRef]

31. Li, S.; Han, S.; Wang, J.; Han, X.; Zheng, P.; Cui, C.; Gao, X.; Sun, S. Infrared thermography detection of grouting defects in external post-tensioned tendon ducts under construction hydration heat excitation. *NDT E Int.* **2023**, *134*, 102785. [CrossRef]

32. Yang, H.; Liu, W.; Wei, D.; Wang, G.; Shen, J. Study on the Detection of the Compactness of Concrete Filled Steel Tube with Model Temperature Difference. *China Concr. Cem. Prod.* **2018**, *5*, 78–81. (In Chinese)

33. Cheng, C.; Cheng, X.; Zhang, H.; Cai, H.; Zhou, J.; Na, R.; Wu, B. Experimental study on infrared detection of debonding in concrete-filled steel tubular structure under acceleratory period of hydration heat action. *Case Stud. Constr. Mater.* **2024**, *21*, e03928. [CrossRef]

34. Cai, H.; Cheng, C.; Wang, L.; Zhang, H.; Zhou, J.; Na, R.; Wu, B. Numerical and experimental study on the evolution of thermal contrast for infrared detection of debonding in concrete filled steel tubular structure. *Appl. Therm. Eng.* **2025**, *258*, 124743. [CrossRef]

35. Cai, H.; Cheng, C.; Na, R.; Zhang, H.; Zhou, J.; Jing, S.; Miao, C. Cooling-excited infrared thermography for enhancing the detection of concrete filled steel tube interfacial debonding at concrete hydration. *Case Stud. Constr. Mater.* **2024**, *20*, e02995. [CrossRef]

36. Rini, D.P.; Chen, R.-H.; Chow, L.C. Bubble behavior and nucleate boiling heat transfer in saturated FC-72 spray cooling. *J. Heat Transf.* **2002**, *124*, 63–72. [CrossRef]

37. Selvam, R.P.; Lin, L.; Ponnappan, R. Direct simulation of spray cooling: Effect of vapor bubble growth and liquid droplet impact on heat transfer. *Int. J. Heat Mass Transf.* **2006**, *49*, 4265–4278. [CrossRef]

38. Sellers, S.M. *Heat Transfer Resulting from the Evaporation of Liquid Droplets on a Horizontal Heated Surface*; Georgia Institute of Technology: Atlanta, GA, USA, 2000.

39. Pais, M.; Chow, L.; Mahefkey, E. Surface roughness and its effects on the heat transfer mechanism in spray cooling. *J. Heat Transf.* **1992**, *114*, 211–219. [CrossRef]

40. Zhibin, Y.; Rui, Z.; Fei, D.; Teck Neng, W.; Kok Chuan, T.; Kok Fah, C.; Poh Keong, C.; Yong Sheng, C. Spray Cooling. In *Two Phase Flow, Phase Change and Numerical Modeling*; Amimul, A., Ed.; IntechOpen: Rijeka, Croatia, 2011; Chapter 13.

41. Omer, K.; Ashgriz, N. Spray Nozzles. In *Handbook of Atomization and Sprays: Theory and Applications*; Ashgriz, N., Ed.; Springer: Boston, MA, USA, 2011; pp. 497–579.

42. Mikhailov, G.K. Chapter 9—Daniel Bernoulli, Hydrodynamica (1738). In *Landmark Writings in Western Mathematics 1640–1940*; Grattan-Guinness, I., Cooke, R., Corry, L., Crépel, P., Guicciardini, N., Eds.; Elsevier Science: Amsterdam, The Netherlands, 2005; pp. 131–142.

43. Hiroyasu, H.; Arai, M.; Tabata, M. Empirical Equations for the Sauter Mean Diameter of a Diesel Spray. *SAE Trans.* **1989**, *98*, 868–877.

44. Kowalczuk, P.B.; Drzymala, J. Physical meaning of the Sauter mean diameter of spherical particulate matter. *Part. Sci. Technol.* **2016**, *34*, 645–647. [CrossRef]

45. Tanasawa, Y. On the atomization of liquid jet issuing from a cylindrical nozzle. *Technol. Rep. Tohoku Univ.* **1955**, *19*, 135.

46. Harmon, D.B. Drop sizes from low speed jets. *J. Frankl. Inst.* **1955**, *259*, 519–522. [CrossRef]

47. Merrington, A.C.; Richardson, E.G. The break-up of liquid jets. *Proc. Phys. Soc.* **1947**, *59*, 1. [CrossRef]